GEOPHYSICS, VOL. 65, NO. 1 (JANUARY-FEBRUARY 2000); P. 304–320, 23 FIGS.

3-D broad-band estimates of reflector dip and amplitude

Kurt J. Marfurt* and R. Lynn Kirlin‡

ABSTRACT

Estimates of seismic coherence of 3-D data sets have provided a radically new way of delineating detailed structural and stratigraphic features. Covariance matrices provide the natural formalism to extend the original three-trace crosscorrelation algorithm to larger analysis windows containing multiple traces, thus providing greater fidelity in low signal-to-noise environments. By use of 3-D phase compensation using Radon transforms, we exploit advances made in the high-resolution multiple signal classification (MUSIC) algorithms, originally developed for the defense industry.

All three families of multitrace attributes (coherence, amplitude, and phase) are coupled through the underlying geology, such that we obtain three families of complimentary images of geologic features that result in lateral changes in wave form. The phase attributes of dip/azimuth and curvature allow us to image areas that have undergone folding or draping that can not be seen on coherence or amplitude images. The amplitude attributes allow us to image oil/water contacts or other areas of amplitude variation that may not be seen on coherence or dip/azimuth images.

Coupled with coherence and the conventional seismic data, these new multitrace dip and amplitude data cubes can greatly accelerate the interpretation of the major features of large 3-D data volumes. At the reservoir scale, they will be of significant help in delineation of subtle internal variations of lithology, porosity, and diagenesis. In computer-assisted interpretation, we strongly feel these new attributes will become the building blocks for the application of modern texture analysis and segmentation algorithms to the delineation of geologic features.

INTRODUCTION

The coherence cube developed by Bahorich and Farmer (1995, 1996) provides a radically new way of extracting detailed structural and stratigraphic features from 3-D seismic data volumes. This original (C1) coherence algorithm, which is based on the normalized crosscorrelation of three adjacent traces, is computationally efficient and provides high spatial resolution of lateral changes in geology when dealing with high-quality seismic data. Unfortunately, this algorithm does not readily generalize beyond three traces, such that the algorithm in general gives poor estimates of coherence and highly erratic estimates of reflector dip and azimuth when dealing with noisy data. The most obvious means of ameliorating this signal-to-noise problem is to increase the number of traces in the analysis window beyond three. In the second generation, or C2, coherence algorithm, Marfurt et al. (1998) present a brute force estimate of these 3-D attributes using a 3-D semblance search over a discrete number of predetermined dip/azimuth pairs. Gersztenkorn and Marfurt (1999) in their multitrace time-domain eigenstructure, or C3, coherence algorithm, further improve coherence estimation by excluding the noise component of the data in the calculation. Although having higher resolution than the semblance algorithm, this original eigenstructure analysis did not search explicitly over reflector dip, so low-coherence artifacts were generated in areas of high structural dip. This problem recently has been circumvented by the generation of a hybrid algorithm that estimates local reflector dip using the more economical, but lower resolution semblance algorithm, smoothing these dips over a large window, and finally calculating the coherence along the smoothed dip direction in our C3.6 coherence algorithm (Marfurt et al., 1999).

Finn (1986) developed perhaps the first 3-D volume-oriented dip/azimuth algorithm and applied it to a grid of 2-D lines. His method explicitly calculates phase lags between adjacent in-line and cross-line traces and, as such, is quite sensitive to noise. The difference algorithm developed by Luo et al. (1996) falls somewhere between our C1 normalized crosscorrelation

Manuscript received by the Editor September 28, 1998; Revised manuscript received March 23, 1999.
*Formerly Amoco EPTG, P. O. Box 3385, Tulsa, Oklahoma 74102-3385; presently University of Houston, Allied Geophysics Lab, Department of Geosciences, 4800 Calhoun Road, Houston, Texas 77204. E-mail: kmarfurt@uh.edu.
‡University of Victoria, ECE Department, 4821 Maplegrove St., Victoria, British Columbia V8Y 3B9, Canada. E-mail: kirlin@sirius.uvic.ca.

Table of symbols

$d_\ell(x, y) = d(f_\ell, x, y)$	= the complex-valued Fourier components of the seismic data
$d_\ell^H(x, y)$	= the complex conjugate transpose of $d_\ell^H(x, y)$
f_ℓ	= the ℓth radial frequency measured in hertz
f_R	= a convenient reference frequency
x_j	= the in-line trace location of the jth trace, measured from the center of the analysis window in meters
y_j	= the cross-line trace location of the jth trace, measured from the center of the analysis window in meters
a	= the amplitude or modulus of $d(f, x_j, y_j)$
ψ	= the phase of $d(f, x_j, y_j)$
p	= the in-line apparent dip measured in milleseconds per meter
q	= the cross-line apparent dip measured in milleseconds per meter
$\mathbf{C} = E(\mathbf{dd^H})$	= the data covariance matrix
λ_j	= the jth eigenvalue of $\mathbf{C}$
$\mathbf{v_j}$	= the eigenvector corresponding to the jth eigenvalue of $\mathbf{C}$
α_i	= coefficients of a paraboloid used to fit the amplitude of the eigenvector $\mathbf{v_1}$
β_i	= coefficients of a paraboloid used to fit the phase of the eigenvector $\mathbf{v_1}$
$\mathbf{A}, \mathbf{B}$	= coefficient matrices used in the least-squares fitting of α_i and β_i to $\mathbf{v_1}$
$\mathbf{I}$	= the identity matrix
ε	= a small number introduced to stabilize the normal equations used to obtain $\mathbf{B}$
x_ξ	= an axis rotated ξ degrees from the in-line (x) axis
p_ξ	= the apparent dip measured along an azimuth of ξ degrees from the in-line (x) axis
t_h	= time of a picked seismic horizon
$\psi_h = 2\pi f_R t_h$	= the phase of the picked time horizon corresponding to the reference frequency f_R
$\rho = \nabla^2 \psi_h$	= the reflector curvature
$\hat{d}\,(m_t, m_x, m_y)$	= seismic data time samples measured at $= m_t \Delta t$, $x = m_x \Delta x$, $y = My\Delta$
$d_\ell = (m_x, m_y)$	= the complex-valued Fourier components of the seismic data corresponding to $f = \ell \Delta f$, $x = m_x \Delta x$ $y = m_y \Delta y$
$\mathbf{L}_\ell$	= the 3-D Radon transform matrix corresponding to $f = \ell \Delta f$
$\mathbf{L}_\ell^\mathbf{H}$	= the complex conjugate transpose of $\mathbf{L}_\ell$
$m_\ell(n_p, n_q)$	= the 3-D Radon transform coefficients or model parameters corresponding to $f = \ell \Delta f$, $p = n_p \Delta p$, $q = n_q \Delta q$
$\bar{\mathbf{d}}_\ell(m_x, m_y)$	= the complex-valued Fourier components of the seismic data, phase corrected from $f = \ell \Delta f$ to f_R
$\mathbf{D_{R\ell}} \equiv \mathbf{L_R}(\mathbf{L}_\ell \mathbf{L}_\ell + \varepsilon \mathbf{I})^{-1} \mathbf{L}_\ell$	= the phase compensation matrix
$\mathbf{r}_n \equiv r(m_x, m_y, p_n, q_n)$	= a plane-wave test function
c_n	= the coherence measured along the dip of the test function $\mathbf{r_n}$
$Tr(\mathbf{C}) = \sum_{j=1}^{J} C_{jj}$	= the numerical trace of $\mathbf{C}$
$c = \lambda_1 / Tr(\mathbf{C})$	= the coherence calculated using the eigenstructure of the phase-compensated covariance matrix
$(k_x, k_y) = (2\pi f p, 2\pi f q)$	= wavenumbers in the x and y directions

algorithm and the amplitude-variation attribute described in this paper. In one implementation, Luo et al. (1996) calculate the variance of the amplitude about the mean within an analysis window. Expansion of these terms includes an unnormalized crosscorrelation of each trace with the mean trace as well as some additional amplitude terms. They estimate dip and azimuth using a slant stack search that is not unlike our semblance search in our C2 coherence algorithm. Luo et al.'s (1996) derivative algorithm is quite different from the coherence family of algorithms, being based on analytic trace analysis in the in-line and cross-line directions.

We have extended the narrow band multiple signal classification (MUSIC) algorithm, developed by Wax et al. (1984) for use in tracking bearing of ships and aircraft from sonar or ground-based antenna arrays, to broad band seismic data. This fifth coherence algorithm, which has proven to be particularly tedious to implement, performs an eigenstructure analysis of the covariance matrix generated from the Fourier-transformed or frequency-domain components of the seismic data within the analysis window. Since the phase component of the complex data array is a measure of time delay or moveout, it was hoped that by calculating the covariance matrices in the frequency domain we could avoid explicitly searching for reflector dip, thereby resulting in a much more efficient algorithm. In this paper, we evaluate the sensitivity of coherence measurements generated by the broadband MUSIC algorithm to geologic faults as well as lateral variations in stratigraphy. More importantly, we develop new 3-D seismic attributes that estimate continuous (versus discrete) estimates of dip/azimuth and curvature, as well as continuous estimates of the lateral variation of reflector amplitude along these dip/azimuth estimates.

THE C5 COHERENCE ALGORITHM

The MUSIC algorithm developed by Wax et al. (1984) is a maximum likelihood estimate of direction of arrival. Although highly effective in tracking narrowband signals from submarine propellers and other sources, this algorithm had not been successfully or efficiently applied to broadband data until recent advances made by Allam and Moghaddamjoo (1994). In Appendices A and B, we extend their treatment to 3-D (t, x, y) or (z, x, y) seismic data cubes. For accurately migrated seismic data, we can simplify their original assumptions by assuming only one reflector lies in the analysis window. This assumption will be valid except along a limited number of unconformities, fault boundaries, and generally incoherent regions of the data.

Maximum coherence exists among all traces when they are time-aligned to the plane of the reflector. Our generalized MUSIC algorithm provides a means of testing all possible dips and azimuths for maximum coherence while simultaneously aligning the wavefronts.

We begin by transforming to the temporal frequency domain using a discrete Fourier transform at a selected number of frequencies. A planar reflector $d(f, x, y)$ in the temporal frequency domain will have the form

$$d(f, x, y) = a\cdot\exp[i\psi(f, x, y)] = a\cdot\exp[i2\pi f(px+qy)], \tag{1}$$

where f is the temporal frequency (measured in hertz), a is the amplitude of the plane-wave event, ψ is the phase of the plane-wave event, x and y are the spatial distances to the center of the analysis window, and p and q are the apparent dips of the planar reflector in the x and y directions (measured in milleseconds per meter).

Each frequency component contains an exponential delay factor $\psi(f, x, y)$ which in turn indicates the apparent dips of the assumed plane event. This delay factor $\psi(f, x, y)$ will vary linearly not only with spatial distance from the center of the analysis window but also with frequency. The MUSIC algorithm allows us to construct a covariance matrix from sample vectors, one vector for each frequency, with each vector element extracted from each trace, thus generating a statistically robust estimate of the covariance matrix. Clearly, a correction to the phase delay ψ needs to be made such that all frequencies will add constructively for consistent apparent dips (p, q). Although the literature (Kirlin and Done, 1999) has given us several means of transforming one frequency's coefficient to another's, none of these have proven to be particularly efficient or robust. We achieve this broad band phase compensation by use of the discrete Radon transform, details of which can be found in Appendix A.

The simplest, most accurate means of phase compensation is to literally time shift all traces according to each trial dip and azimuth before calculating the covariance matrix. This is exactly what is done in the time domain semblance or C2 algorithm developed by Marfurt et al. (1998) and the hybrid time domain semblance–eigenstructure or C3.6 algorithm developed by Marfurt et al. (1999). These algorithms do not require Fourier transformation; rather, the covariance matrix can be directly obtained using vectors extracted from time interpolated analytic traces. In contrast, the MUSIC algorithm implements this time shift as a phase shift in the frequency domain by simply multiplying the sample vector by $\exp[i\Delta\psi(x, y, f)]$ for each trial direction. By avoiding temporal interpolation before creating the covariance matrix, we improve computational efficiency. MUSIC is both a high resolution and a subspace algorithm—subspace meaning that most noise dimensions of the data (corresponding to the smaller eigenvalues) are ideally excluded from the calculations of the parameters of interest. According to theory, considerable gains in angular resolution are made when the signal-to-noise ratio is above a critical threshold.

EIGENVALUE ANALYSIS: CALCULATION OF COHERENCE

Figure A-1 in Appendix A shows a typical analysis window incorporating J traces. Applying the minimum variance, distortionless response (MVDR) analysis of the corresponding J by J covariance matrix, $\mathbf{C}$, described in Appendix B, generated from the broadband phase-compensated data extracted from the trace analysis window, we obtain our estimate of coherence c (equation B-8):

$$c = \frac{\lambda_1}{Tr(\mathbf{C})}, \tag{2}$$

where λ_1 denotes the largest of the J eigenvalues and $Tr(\mathbf{C})$ denotes the sum of diagonal elements of the matrix $\mathbf{C}$.

As with our C1, C2, C3, and C3.6 coherence algorithms, the value of coherence c for the C5 algorithm has been constructed to always range between 0 and 1. In Figure 2, we compare all five coherence algorithms for the time slice shown in Figure 1a, centered about a salt dome in the Gulf of Mexico, offshore Louisiana. With the exception of the 3-trace C1 algorithm, all coherence estimates were calculated using the same 5-trace (12.5 m × 25 m) operator and the same ±40-ms vertical window centered about the time slice at 1200 ms. The C2 algorithm explicitly searched over some 32 (dip, azimuth) pairs. These dips (Figure 3) were smoothed over a 100 m × 100 m window and used to guide our C3.6 algorithm. The C5 algorithm used five frequencies spaced equally between 12.5 and 62.5 Hz at 12.5 Hz increments, phase compensated to 25 Hz. The relative computational effort of these four algorithms is displayed in Figure 4.

Arrows indicate subtle variations in coherence between these four algorithms. First, we note that the frequency domain C5 algorithm implicitly takes into account variations of dip that are not honored by our time domain eigenstructure C3 algorithm, so we can interpret faults that cut the steeply dipping flanks of the salt dome. Nevertheless, the C5 algorithm appears to be inferior to the hybrid C3.6 algorithm in this same zone, with the C5 algorithms estimate of coherence having considerably reduced lateral resolution and continuity of fault traces. Thus, we have developed an algorithm that is somewhat inferior in quality, but computationally more expensive than the hybrid C3.6 algorithm. In addition, since the Fourier transform of the various frequency components requires a vertical analysis window whose length is equal to the reciprocal of the lowest frequency to be used, this algorithm will by necessity have less vertical resolution than our time domain semblance algorithm, which can operate on as few as one sample in the analysis window.

EIGENVECTOR ANALYSIS: CALCULATION OF LATERAL VARIATION OF REFLECTOR DIP AND AMPLITUDE

In this section, we examine the usefulness of the first eigenvector $\mathbf{v_1}$ or principal component of the frequency domain covariance matrix $\mathbf{C}$ described in Appendix B. This unit length eigenvector $\mathbf{v_1}$ is a necessary by-product in the calculation of the largest eigenvalue λ_1 using the efficient Rayleigh product method (Golub and van Loan, 1983). By definition, the principal component represents that complex-valued lateral variability across J traces that best represents the lateral variability in the complex (phase-compensated) data vectors for each frequency that contributed to the covariance matrix $\mathbf{C}$. If we were to subtract the principal component from the phase compensated data vectors $\bar{\mathbf{d}}_\ell$, thereby forming a residual vector for each frequency, the second principal component would be that complex waveform that best represents these residual vectors, yet is orthogonal to the first principal component.

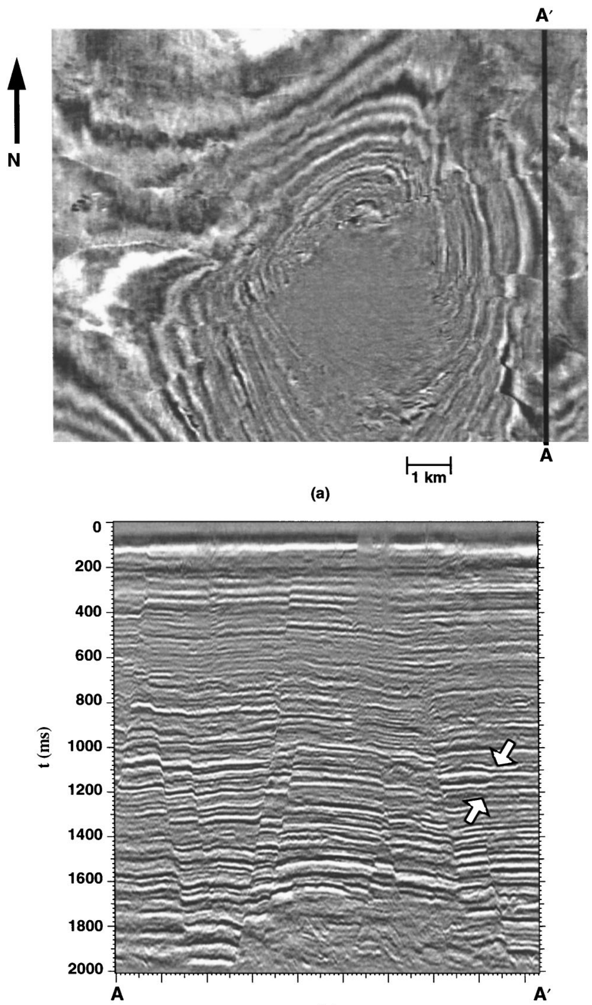

FIG. 1. Data through a salt done from the Gulf of Mexico: (a) a time slice through a seismic data volume at $t = 1200$ ms and (b) a vertical slice along AA′. Arrows indicate a small flexural feature at $t = 1200$ ms. Data courtesy of Geco-Prakla.

Although our discussion in Appendices A and B postulated a simple plane-wave reflector across the analysis window having the form of equation (1), this by no means requires that the principal component eigenvector calculated from the actual data will be planar in form. We therefore find it useful to decompose the complex-valued principal component eigenvector $\lambda_1\mathbf{v_1}$ into two real vectors of amplitude $\mathbf{a}$ and phase ψ, using

$$\lambda_1 v_1(x_j, y_j) = a(x_j, y_j)\exp[i\psi(x_j, y_j)], \tag{3}$$

where (x_j, y_j) are the coordinates of the jth trace within the analysis window.

We then parameterize the variation in amplitude and phase to be parabolic in (x, y):

$$a(x, y) = \alpha_0 + \alpha_1 x + \alpha_2 y + \alpha_3 x^2 + \alpha_4 xy + \alpha_5 y^2, \tag{4}$$

and

$$\psi(x, y) = \beta_0 + \beta_1 x + \beta_2 y + \beta_3 x^2 + \beta_4 xy + \beta_5 y^2. \tag{5}$$

The phase coefficients have ready physical interpretations: β_1 and β_2 correspond to a broadband estimate of p and q, the apparent dips in the x and y directions given in equation (1), whereas coefficients β_3 and β_5 are estimates of the reflector curvature in the x and y directions. Calculation of the eigenvector $\mathbf{v_1}$ is indeterminate with respect to a constant phase factor (Kirlin and Done, 1999), so the value of β_0 is useless for interpretation.

To our knowledge, the amplitude coefficients α_j are somewhat new to seismic analysis, but are nevertheless easy to understand. Coefficient α_0 is simply a multitrace estimate of the broadband reflectivity at the center of the analysis window. Coefficients α_1 and α_2 are the change in variation of the reflectivity in the in-line (x) and cross-line (or y) directions. Similarly, α_3 and α_5 are the rate of change, or second derivative, of these amplitudes in the x and y directions.

If we rewrite equations (4) and (5) as a J by 5 matrix equation for each of the J or more traces in the analysis window in the form

$$\mathbf{a} = \mathbf{A}\alpha, \tag{6}$$

and

$$\psi = \mathbf{A}\beta, \tag{7}$$

we can solve for α and β using conventional least squares:

$$\alpha = (\mathbf{A^T A} + \varepsilon\mathbf{I})^{-1}\mathbf{A^T a}, \tag{8}$$

and

$$\beta = (\mathbf{A^T A} + \varepsilon\mathbf{I})^{-1}\mathbf{A^T}\psi, \tag{9}$$

where $\mathbf{I}$ is the identity matrix, ε is a small positive number introduced for numerical stability, and the superscript T denotes the transposed matrix.

Since the analysis window does not change with spatial or temporal position, we simply precompute the matrix $\mathbf{B}$:

$$\mathbf{B} = (\mathbf{A^T A} + \varepsilon\mathbf{I})^{-1}\mathbf{A^T}, \tag{10}$$

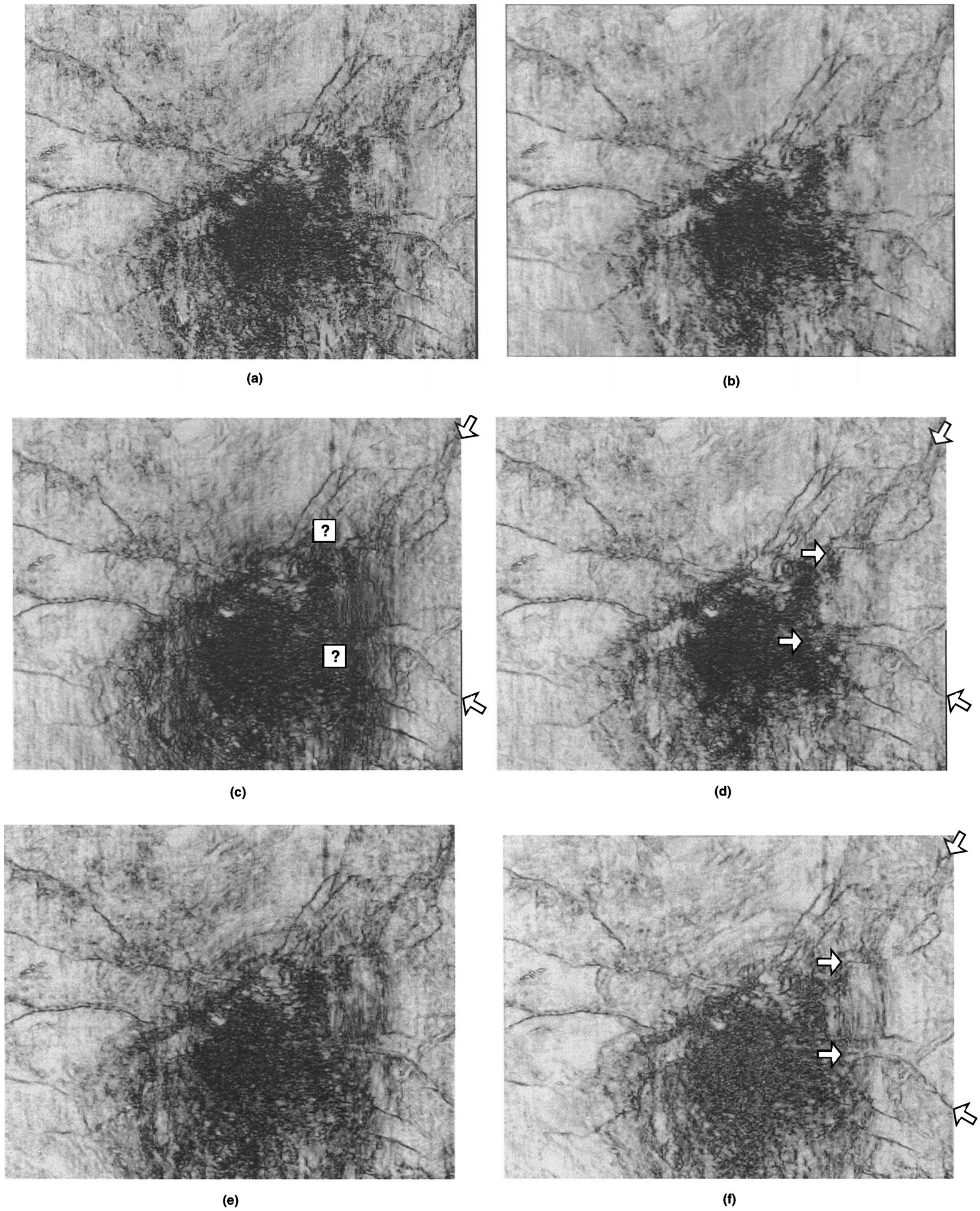

FIG. 2. Time slices at $t = 1200$ ms through coherence cubes produced using six different algorithms: (a) C1—cross correlation, (b) C2—time domain semblance, (c) C3—time domain eigenstructure with no dip search, (d) C3.6—hybrid time domain semblance–eigenstructure with a dip search, (e) MUSIC without phase compensation, and (f) C5—MUSIC with phase compensation. Arrows indicate faults that are difficult to follow through the steep areas using the C3 algorithm. Even so, the C5-generated coherence has less resolution than either C3 or C3.6.

and apply it to all eigenvectors $\mathbf{v_1}$ estimated in the seismic volume, providing us with several useful attributes at only a small additional cost to our C5 algorithm estimate of coherence c.

DISCUSSION

In Figure 5, we show the apparent dip in the in-line and cross-line directions, as well as intermediate apparent dips p_ξ along the x_ξ-axis, rotated by an angle ξ from the x-axis given by

$$\frac{\partial\psi}{\partial x_\xi} = p_\xi = p\cos\xi + q\sin\xi, \tag{11}$$

for the same time slice at 1200 ms shown in Figures 1–3. (We could just as easily have displayed dip and azimuth as discussed in Marfurt et al., 1998.) Several aspects of the data are immediately apparent that are not obvious from the coherence slices alone. First, one is easily able to envision the structural dip from the apparent shadows generated by this eigenvector decomposition. This continuous estimate of reflector dip is consistent with, but has significantly greater resolution than, the discrete dip estimates generated by our C2 algorithm in Figure 3.

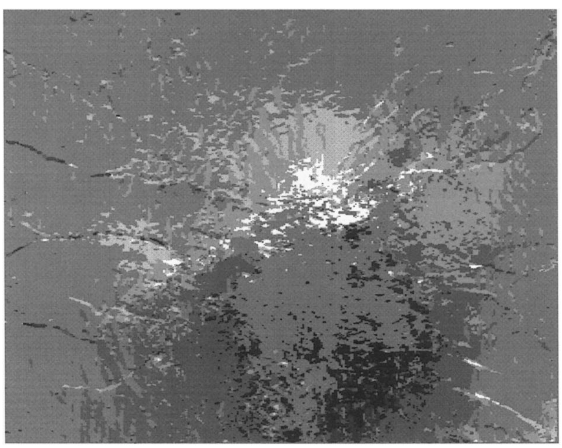

(a)

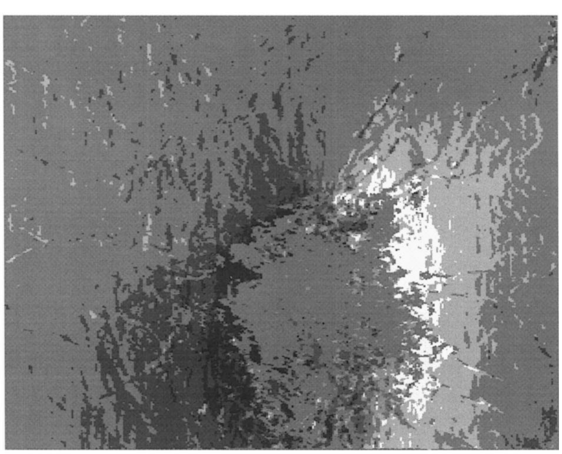

(b)

FIG. 3. Apparent dips, p_ξ, estimated for (a) $\xi = 0^\circ$, and (b) $\xi = 90^\circ$, using the discrete dip search used in C2 or semblance algorithm at time slice $t = 1200$ ms.

Second, due to this increased resolution, we are able to delineate subtle flexural features that are less obvious on the coherence data. As an example, we notice a flexural feature on line AA′ at 1200 ms in Figure 1b that lies just above a major fault. This fault-associated flexure or drape appears quite diffuse on our coherence slices (Figure 2), but is clearly visible on the dip slices in Figure 5. In map view, we see a relationship between the west end of this flexural feature and the north end of a clearly defined radial fault. Care must be taken in the interpretation of these apparent dip images. They are "apparent" not only in the traditional geologic sense of being the true dip projected onto the transept, but also in the literal sense, in that they may only "appear" to be dips, but are rather finite offsets across a fault.

The coefficient of xy (β_4) is underdetermined for the $J = 5$ trace analysis window used in this example. To our knowledge, this estimate is not commonly used in structural interpretation, but is equivalent to the skewness coefficient used in texture and segmentation analyses (Wu and Doerschuk, 1994).

For the sake of simplicity, we combine the vector curvature components β_3 and β_5 (the coefficients of x^2 and y^2, respectively) into a single attribute which we will simply call the reflector curvature, ρ:

$$\rho = \nabla^2\psi = \frac{\partial^2\psi}{\partial x^2} + \frac{\partial^2\psi}{\partial y^2} = \beta_3 + \beta_5, \tag{12}$$

and display the result in Figure 6. This reflector curvature map is analogous to the edge-detected dip azimuth maps along an interpreted horizon, presented by Mondt (1990). It is dissimilar in that the horizon-edge detection algorithms require an interpreter (or an interpreter guided algorithm) to explicitly pick a geologic horizon, whereas our method [and those of Dalley et al. (1989), Luo et al. (1996) and Marfurt et al. (1998)] can work along either an interpreted horizon, or alternatively along any vertical section, time slice, or depth slice through the seismic data cube prior to interpretation. Like coherence,

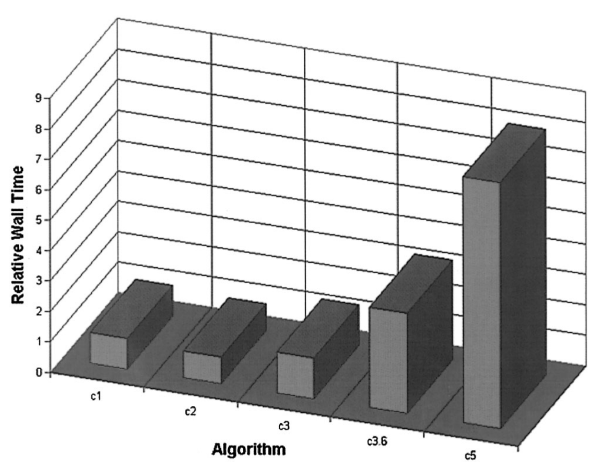

FIG. 4. Relative computational effort on an Ultra Sparc workstation of the coherence algorithms discussed in this paper. With the exception of the 3-trace C1 algorithm, all times correspond to a 5-trace, ±40-ms analysis window.

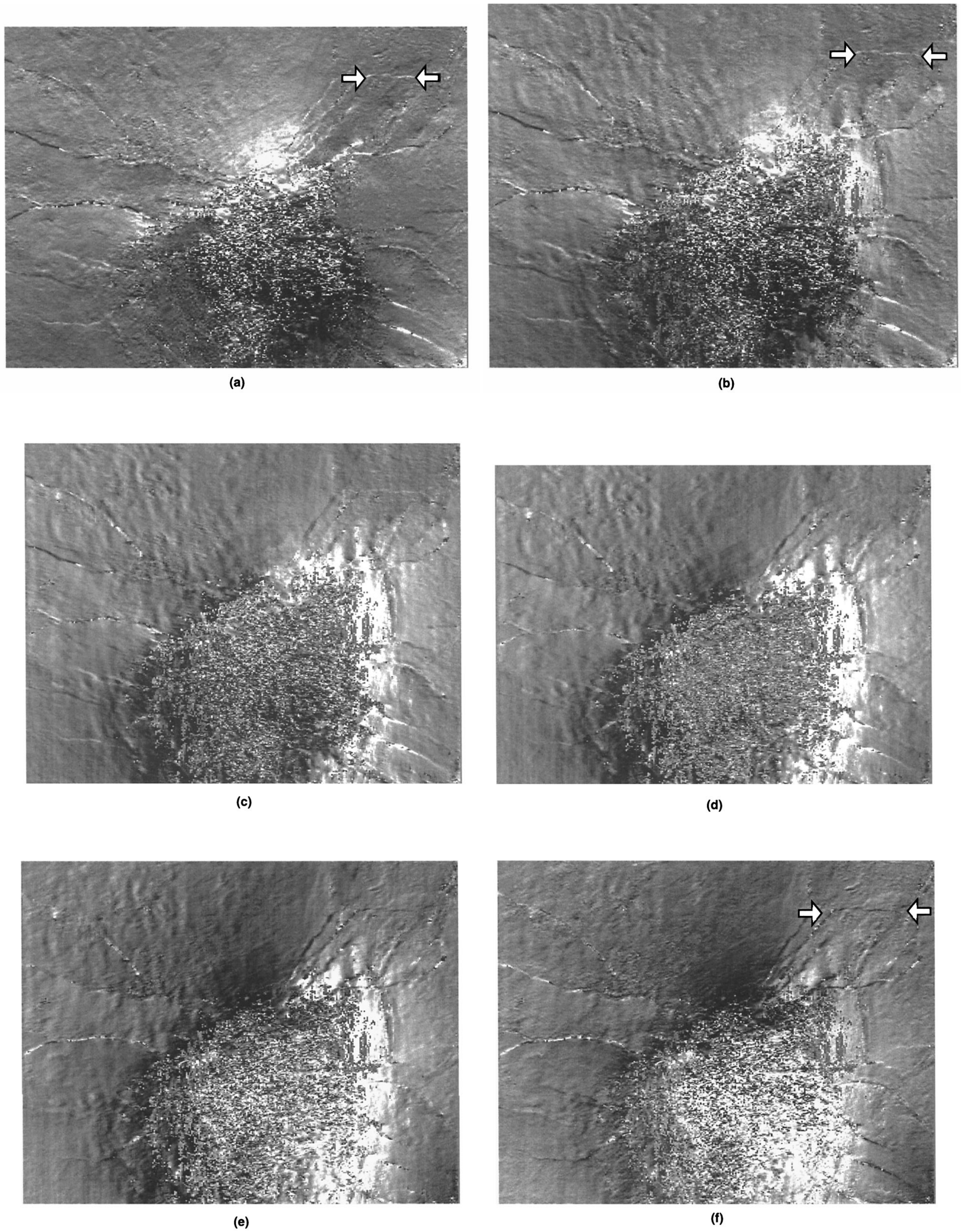

FIG. 5. Apparent dips p_ξ estimated for (a) $\xi = 0°$, (b) $\xi = 30°$, (c) $\xi = 60°$, (d) $\xi = 90°$, (e) $\xi = 120°$, and (f) $\xi = 150°$, using the C5 or phase-compensated MUSIC algorithm at time slice $t = 1200$ ms. White corresponds to positive dip downwards in the direction of ξ. Images generated at 180°, 210°, 240°, 270°, 300°, and 330° would appear as photographic negatives of images (a)–(f). Arrows indicate a small flexural feature denoted on Figure 1b and discussed in the text.

being able to calculate and display reflector dips and curvature prior to interpretation allows us to quickly visualize and generate a structural framework of the earth's subsurface, thereby greatly accelerating the traditional interpretation process.

In Figure 7a, we display the α_0 coefficient of our amplitude expansion, that is, a least-squares J-trace estimate of phase compensated reflectivity at the center of the analysis window. Since the amplitude term in equation (3) is always positive or rectified, it may be somewhat difficult to compare to the traditional data extraction amplitude displayed in Figure 1a. We therefore display the single trace response envelope (Bodine, 1984) in Figure 7b. We note that due to the J-trace versus single trace estimate, the α_0 coefficient is less noisy than the wavelet envelope. We also note that the we have greater lateral resolution of the fault plane discontinuities, complementing our coherence images in Figure 2 and apparent dip and curvature images in Figures 5 and 6.

Of considerably greater interest is the enhanced detail provided by the amplitude gradient images along the x_ξ axis shown in Figure 8, given by

$$\frac{\partial a}{\partial x_\xi} = \alpha_1 \cos\xi + \alpha_2 \sin\xi. \tag{13}$$

These images show the lateral change in amplitude with distance along the azimuth ξ, and is algorithmically independent of the phase variations or apparent dip shown in Figure 5. We note that the amplitude of the incoherent energy at the center of the salt dome is nearly zero. We explain this phenomenon as being due to three processes. First, the original data internal to the salt dome (Figure 1a) were low in amplitude. Second, since our phase compensation was only applied to dipping reflectors up to the spatial Nyquist criterion, more steeply dipping, aliased events are partially attenuated during the forward Radon transform given by equation (A-3). Third, the data inside the salt dome are largely incoherent, so we do not expect our phase compensation algorithm that was defined for coherent, albeit dipping reflectors to produce consistent phase consistent corrected data $\mathbf{d_I}$ given by equation (A-7). The addition of these randomly phased data vectors in our covariance matrix calculation (equation B-1) will result in a principal component $\lambda_1\mathbf{v_1}$, whose magnitude tends towards zero. For completeness, we display the Laplacian of the amplitude coefficient in Figure 9, given by

$$\nabla^2 a = \frac{\partial^2 a}{\partial x^2} + \frac{\partial^2 a}{\partial y^2} = \alpha_3 + \alpha_5. \tag{14}$$

This image provides a third means of edge detection that is numerically independent of coherence and reflector curvature.

Since there are no bright spot amplitude events of interest in Figure 1, we examine a volume of data from a different part of this survey that was flattened along an irregular geologic horizon (Figure 10) containing some of the major distributary features of the paleo–Mississippi River (Figure 11). We have chosen these data since the geologic features are interpretationally easy to visualize, and since we have strong reflectivity contrasts between the sand prone channels and the shale

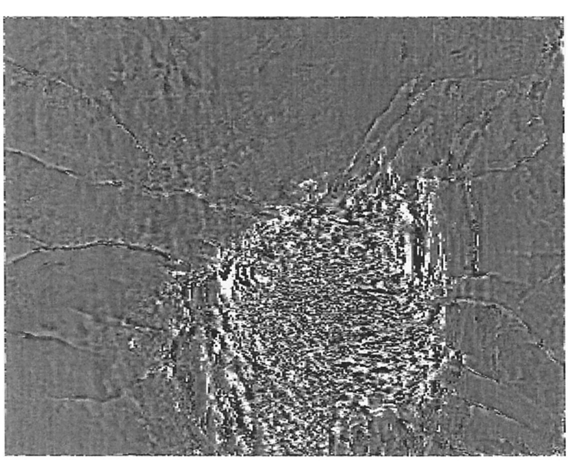

FIG. 6. $\nabla^2\psi = \partial p/\partial x + \partial q/\partial y$, generated at time slice $t = 1200$ ms. Compare this phase-based edge-detection image to the coherence-based edge-detection images shown in Figure 2.

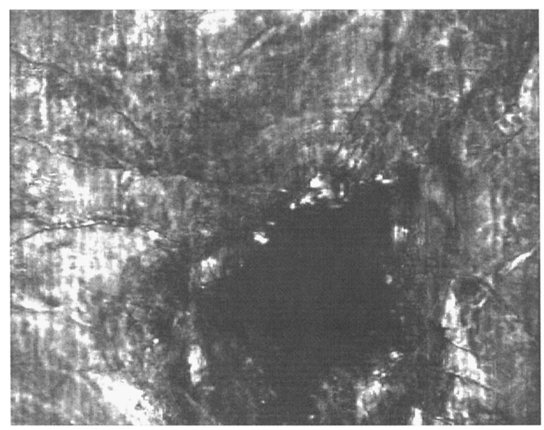

(a)

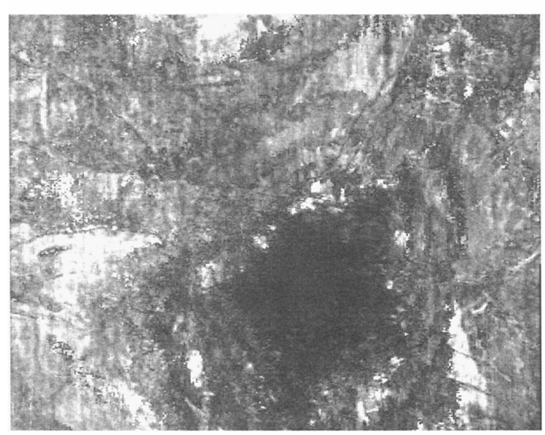

(b)

FIG. 7. (a) Modulus of complex amplitude, estimated at the center of the analysis window, $a(x = 0, y = 0)$, estimated using the C5 MUSIC algorithm. (b) Modulus of conventional complex trace analysis, or response envelope, described by Bodine (1984). White implies high amplitude, black implies low amplitude. Compare both figures to the conventional amplitude extraction shown in Figure 1a.

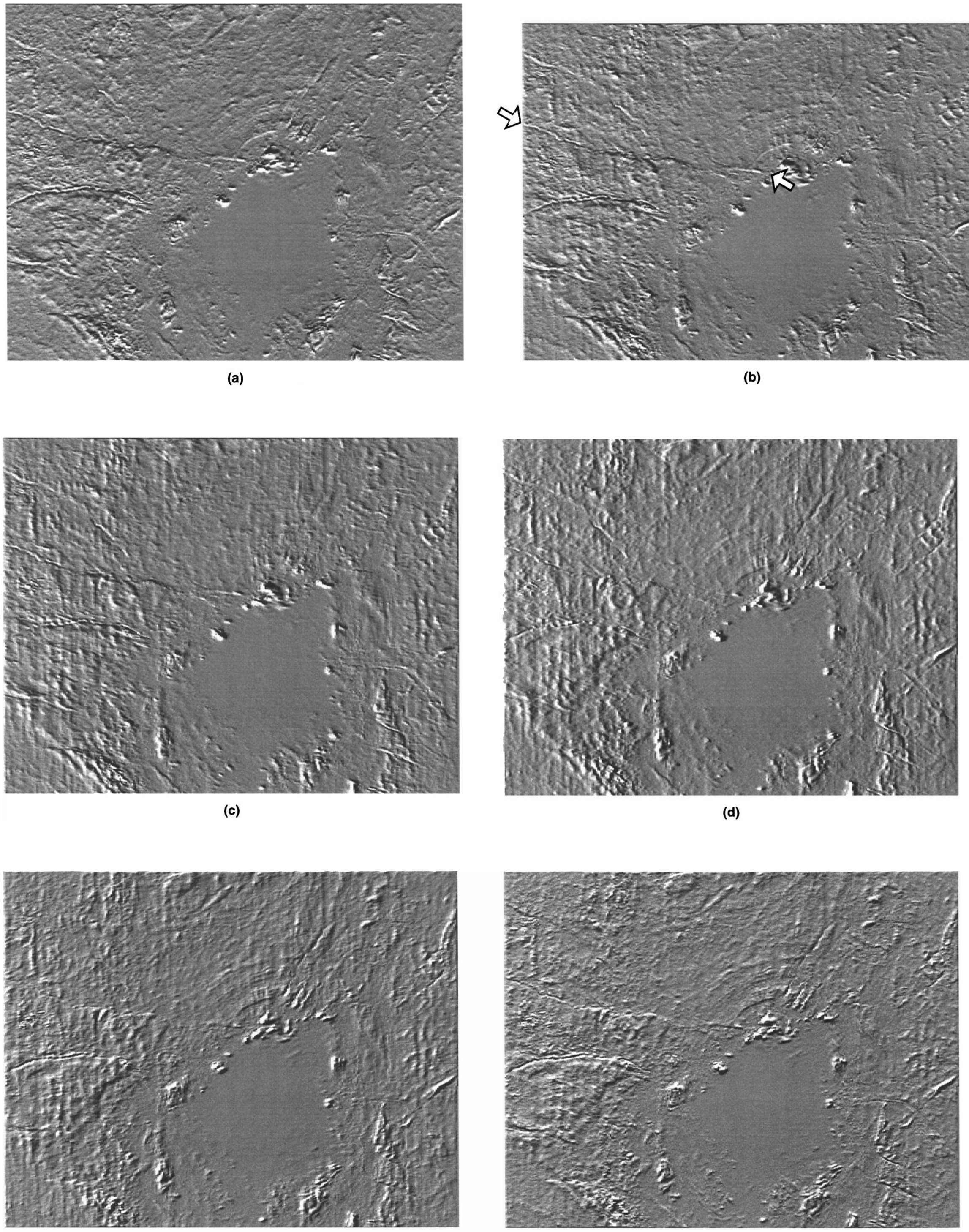

FIG. 8. Gradient of modulus of complex amplitude, $\partial a/\partial\xi$, estimated for (a) $\xi = 0^\circ$, (b) $\xi = 30^\circ$, (c) $\xi = 60^\circ$, (d) $\xi = 90^\circ$, (e) $\xi = 120^\circ$, and (f) $\xi = 150^\circ$. White corresponds to increasing amplitude in the direction of ξ. Arrows indicate a fault which is much more continuous (though the polarity reverses!) than on any of the coherence images shown in Figure 2. Note that the north-south acquisition footprint affects the east-west amplitude gradient in (d) more than the east-west apparent dip in Figure 5d.

prone matrix. The C3 coherence image (Figure 12) run on this data volume after flattening is consistent with this depositional model. The coherence nicely outlines the edges of the channel, though providing little additional detail within.

We display amplitude gradient maps along this horizon at 0° and 90° in Figure 13. Careful comparison shows that there is nothing in Figure 13 that is not in the original time slice of Figure 11. Nevertheless, since we are looking at changes in amplitude, subtle features like the narrow sand channels indicated by arrows leap out at the interpreter in these gradient maps, allowing us to easily visualize and quantify small lateral variations in amplitude. We display the divergence of amplitude $\nabla^2 a$ in Figure 14.

For this example, ψ, the phase of the principal component $\lambda_1 \mathbf{v_1}$ given by equation (3) is calculated with respect to the flattened horizon. Mondt (1990) shows how faults and stratigraphic features can be enhanced by calculating the apparent dips (or alternatively, the dip and azimuth) and curvature of the picks themselves. One major difference between such a "horizon" dip map and the time slices through apparent dip cubes such as shown in Figure 6 is that, like the coherence cube, the apparent dip cube is performed on the data before rather than after interpretation.

While we could calculate apparent dip cubes and extract the apparent dip along the picked horizon, there are situations where we may only wish to calculate attributes along a flattened horizon and nowhere else. In this case, equation (3) gives us an estimate of the reflector phase difference $\Delta\psi_h$ with respect to the flattened horizon. Since the phase ψ_h of the picked horizon

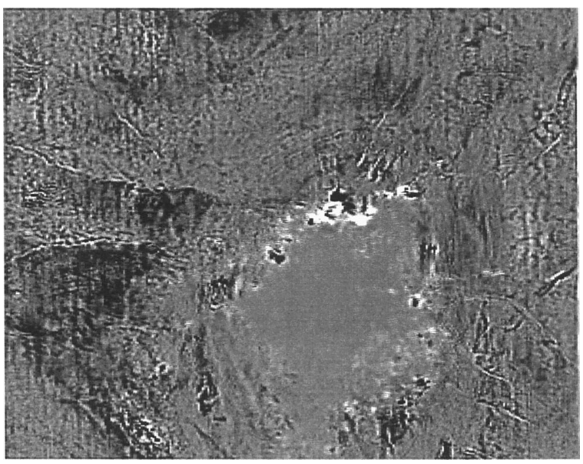

FIG. 9. $\nabla^2 a = \partial^2 a/\partial x^2 + \partial^2 a/\partial z^2$, the divergence of the modulus of the complex amplitude estimated using our C5 MUSIC algorithm. Compare this amplitude-based edge-detecting attribute with the phase and coherence edge-detection attributes shown in Figures 6 and 2.

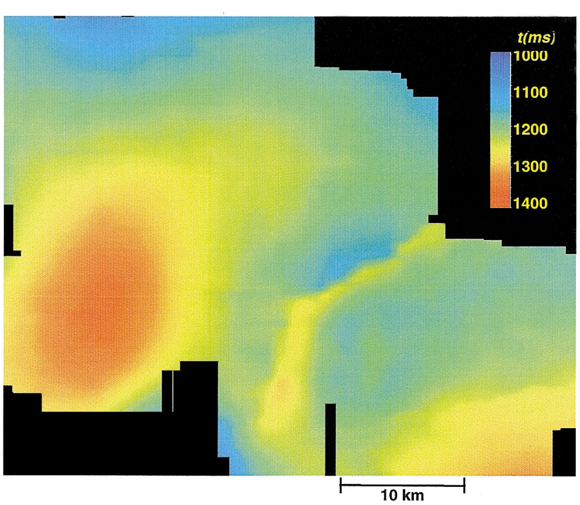

FIG. 10. A smoothed stratigraphic horizon corresponding to the paleo–Mississippi River distributory system.

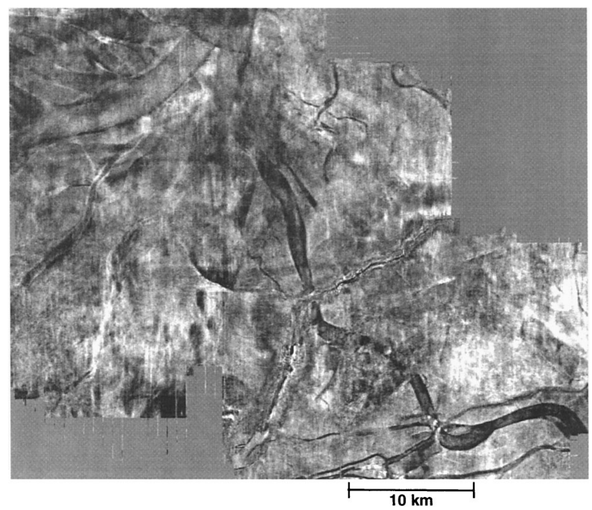

FIG. 11. Conventional amplitude extraction made along the horizon shown in Figure 10. Seismic data courtesy of Geco-Prakla.

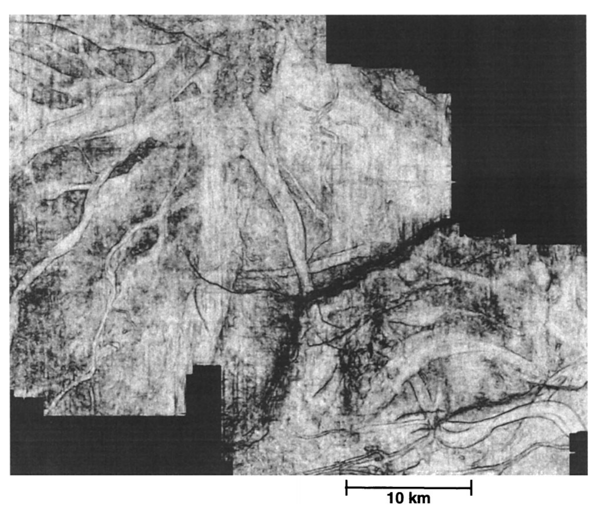

FIG. 12. Seismic coherence estimated using the C3 algorithm corresponding to the amplitude extraction shown in Figure 11, using an 11-trace, ±32-ms analysis window.

at time t_h at the reference frequency f_R is simply

$$\psi_h = 2\pi f_R t_h, \tag{15}$$

the phase of the principal component analysis with respect to time, $t = 0$, would be given by

$$\psi = 2\pi f_R t_h + \Delta\psi_h. \tag{16}$$

If we use this estimate of ψ in equation (9), without including the smooth dip of the interpreted horizon shown in Figure 10, we obtain the apparent dip images shown in Figure 15. The amplitude gradients and divergence displayed in Figures 13 and 14 are calculated along these apparent dips and not along the apparent dip of the picked horizon.

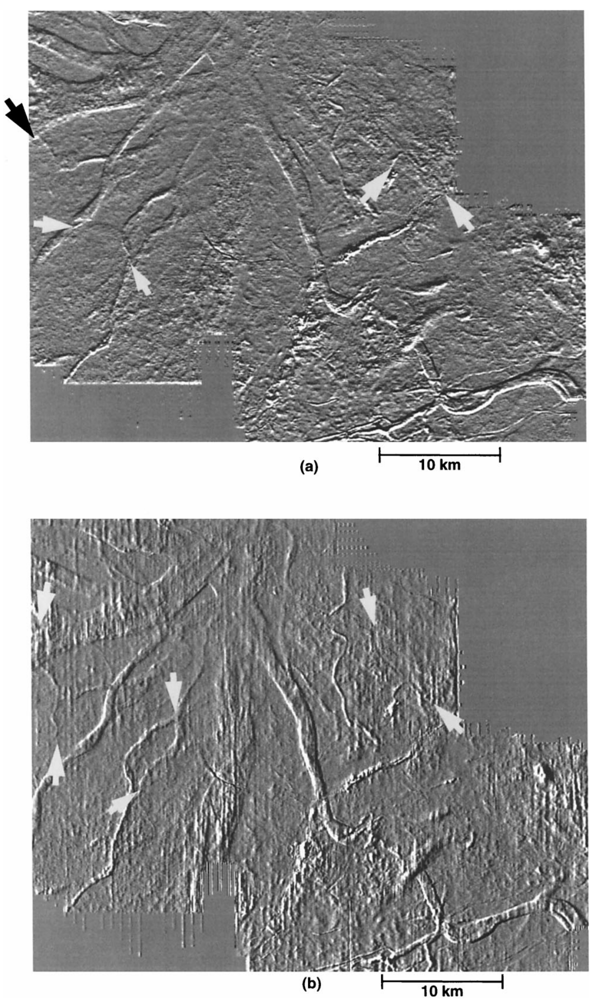

FIG. 13. Gradient of the modulus of the complex amplitude $\partial a/\partial \xi$ along the horizon shown in Figure 10 estimated for (a) $\xi = 0^\circ$, and (b) $\xi = 90^\circ$. White corresponds to increasing amplitude in the direction of ξ. Arrows indicate subtle channel features not readily evident on the amplitude extraction or coherence images in Figures 11 and 12.

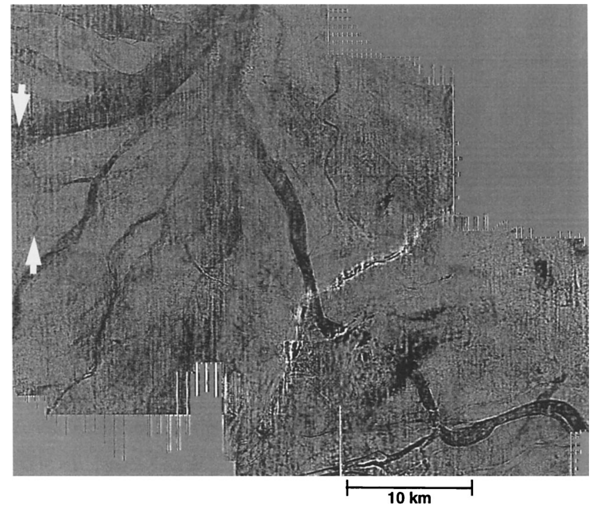

FIG. 14. $\nabla^2 a$, the divergence of the modulus of the complex amplitude along the horizon shown in Figure 10.

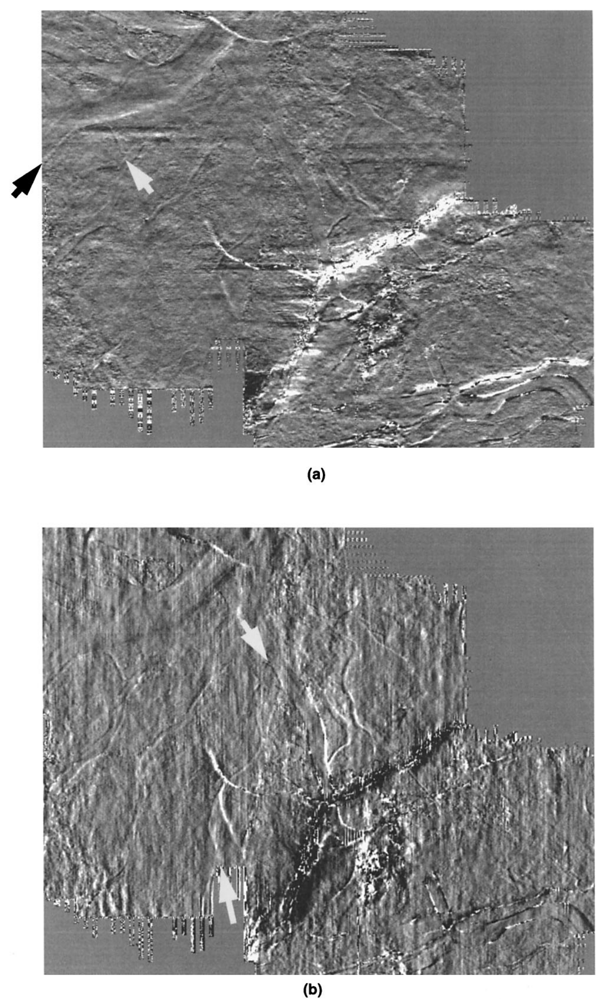

FIG. 15. Apparent dips (a) p_0 to the north and (b) p_{90} to the east relative to the horizon shown in Figure 10.

CONCLUSIONS

In an effort to develop a more efficient eigenstructure-based coherence estimate in the frequency domain using the MUSIC algorithm, we have generated a family of new seismic attributes that quantify subtle variations in reflector dip and amplitude. Although this new C5 estimate of coherence is inferior to our C2 time domain semblance and hybrid C3.6 time domain eigenstructure coherence estimates, our new reflector dip and amplitude attributes hold significant interpretational promise. By calculating the eigenvectors in the complex frequency domain, we obtain an efficient, continuous estimate of apparent dip (or alternatively dip/azimuth) that provides higher resolution than that obtained by our discrete search C2 time domain algorithm. Although these attributes are numerically independent from each other and from coherence, they are often coupled through the causative geology, such that changes in dip, amplitude, and coherence provide complementary images of faults and stratigraphic discontinuities.

More important, these new enhanced estimates of reflector dip and azimuth variation allow us to easily map features that have heretofore required much greater interpretational effort, and where coherence has been of only limited value. Curving reflectors will be mapped as coherent events, yet quantitatively mapping reflector curvature is one of the more effective means of predicting fold deformation-induced fractures. Coherence also fails to provide us necessary detail when the reflected signal is too coherent, such as occurs in large gas-charged bright spots. Being able to map subtle changes in reflector dip and amplitude may allow us to differentiate underlying changes in lithology, such as individual sand lobes in a deltaic sequence, crosscutting channels in a fluvial sequence, or diagenetic barriers that are key to effective reservoir production management.

Our new estimates of apparent dip and amplitude gradient bear a superficial resemblance to the shaded relief maps commonly used in image processing. They differ from shaded relief maps in that they are calculations of phase and amplitude changes within a 3-D volume, rather than amplitude changes along a 2-D surface.

In summary, we have generated more versatile means of analyzing the same data. Apparent dip images allow us to quickly envision 3-D structural relationships from time or depth slices. The amplitude gradient maps allow us to quickly visualize subtle lateral variations in reflectivity. From these we have generated two new edge detector attributes, one sensitive to changes in dip (curvature), the other sensitive to changes in amplitude (such as may occur at a gas/water contact). Coupled with coherence and the conventional seismic data, these additional images will directly translate into greatly accelerated interpretations of the major features of large 3-D data volumes. In contrast, on the reservoir scale, these multiple views of the same small piece of data provide the interpreter more quantitative measures of internal reservoir inhomogeneity. In computer-assisted interpretation, we feel strongly that these new attributes will become the building blocks for the application of modern texture analysis and segmentation algorithms in the delineation of geologic features.

ACKNOWLEDGMENTS

We thank the Amoco Business Units for their support and Jeff Johnson for his strong leadership of Amoco Geoscience Technology throughout the life of our seismic coherence R&D effort.

We also thank Julie Youngblood in Amoco's Tulsa Technology Center's Document Services for her tenacity and exactitude in helping to produce this manuscript. Finally, we thank Frédéric Verhelst for his careful review, leading to improvement of our final paper.

This technology is protected by US Patent 5 940 778.

REFERENCES

Allam, M., and Moghaddamjoo, A., 1994, Two-dimensional DFT projection for wideband direction of arrival estimation: IEEE Signal Processing Letters, **1**, 35–37.

Bahorich, M. S., and Farmer, S. L., 1995, 3-D Seismic discontinuity for faults and stratigraphic features: The coherence cube: The Leading Edge, **14**, 1053–1058.

——— 1996, Methods of seismic signal processing and exploration: U.S. Patent 563 949.

Bodine, J. H., 1984, Waveform analysis with seismic attributes: Geophysics, **50**, 327.

Dalley, R. M., Gevers, E. E. A., Stampli, G. M., Davies, D. J., Gastaldi, C. N., Ruijtenberg, P. R., and Vermeer, G. J. D., 1989, Dip and azimuth displays for 3-D seismic interpretation: First Break, **7**, 86–95.

Finn, C. J., 1986, Estimation of three dimensional dip and curvature from reflection seismic data: M.S thesis, Univ. of Texas at Austin.

Gersztenkorn, A., and Marfurt, K. J., 1999, Eigenstructure-based coherence computations as an aid to 3-D structural and stratigraphic mapping: Geophysics, **64**, 1468–1479.

Golub, G. H., and van Loan, C. F., 1983, Matrix computations: Johns Hopkins Univ. Press.

Kirlin, R. L., and Done, W. E., 1999, Applications of covariance matrices to seismic signal processing: Soc. Expl. Geoph.

Luo, L., Higgs, W. G., and Kowalik, W. S., 1996: Edge detection and stratigraphic analysis using 3-D seismic data: 66th Ann. Internat. Mtg., Soc. Expl. Geophys., Expanded Abstracts, 324–327.

Marfurt, K. J., Kirlin, R. L., Farmer, S. L., and Bahorich, M.S., 1998, 3-D seismic attributes using a running window semblance-based coherency algorithm: Geophysics, **63**, 1150–1165.

Marfurt, K. J., Sudhakar, V., Gersztenkorn, A., Crawford, K. D., and Nissen, S. E., 1999, Coherency calculation in the presence of structural dip: Geophysics, **64**, 104–111.

Mondt, J. C., 1990, The use of dip and azimuth horizon attributes in 3-D seismic interpretation: SPE 20943, 71–77.

Owsley, N., 1985, The MVDR algorithm, *in* Haykin, S., Ed., Array signal processing: Prentice Hall, Inc., 115–193.

Parlett, B. N., 1980, The symmetric eigenvalue problem: Prentice-Hall, Inc.

Wax, M., Shan, T.-J., and Kailath, T., 1984, Spatio-temporal spectral analysis by eigenstructure methods: IEEE Trans. ASSP, **32**, 817–827.

Wu, C., and Doerschuk, P., 1994, Texture based segmentation using Markov random field models and approximate estimators based on trees: J. Math. Imaging and Vision, **5**, 721–741.

APPENDIX A

THE 3-D BROADBAND ALGORITHM

In this appendix, we extend the classical MUSIC scheme to broadband signals by generalizing Allam and Moghaddamjoo's (1994) method to 3-D data volumes, thereby developing a method of spatial sampling such that the phase of each constant frequency gather is consistent for all other frequencies along the reflector dip and azimuth direction. Plane wave decomposition (or 3-D Radon transform techniques) provides a natural way to achieve this broadband phase compensation.

Our analysis operates on an elliptical or rectangular spatial analysis window encompassing J traces, $\hat{d}\,[m_t, m_x(j), m_y(j)]$, extracted from a volume of time or depth migrated data (Figure A-1); m_t, m_x, and m_y denote discrete samples along the t, x, and y axes whose origin is at the center of the analysis window. Subsequent estimates of coherence are achieved by sliding the analysis window to the next time sample in t, or to the next adjacent trace in x or y.

To construct our covariance matrix, we need multiple sample vectors of Fourier coefficients, one vector for each frequency (Kirlin and Done, 1999). We begin by taking the discrete Fourier transform (DFT) at a select number of frequencies, f_ℓ, in a temporal analysis window $(-M_t \le m_t \le +M_t)$ centered about $m_t = 0$:

$$d_\ell(m_x, m_y) = \sum_{m_t=-M_t}^{+M_t} \hat{d}(m_t, m_x, m_y) \exp\left(-i2\pi f_\ell m_t \Delta t\right). \tag{A-1}$$

Let us assume a zero-phase planar reflector of amplitude a and apparent dips p and q, centered about the origin of the analysis window $(m_x = 0, m_y = 0, m_t = 0)$ (Figure A-2). At a reference frequency $f_\ell = f_R$:

$$d_R(m_x, m_y) = a \exp[-i2\pi f_R(pm_x\Delta x + qm_y\Delta y)]. \tag{A-2}$$

We note in Figure A-3 that while the phase at an arbitrary frequency component f_ℓ will match the phase of the component at f_R at the origin $(x = 0, y = 0)$ for a zero-phase wavelet, the phases will not match the phases of the reference frequency for nonzero values of x and y. Instead, we note that each frequency coefficient's phase changes with different slopes as we move away from the origin.

While we may perform this phase compensation in the Fourier, (f, k_x, k_y) domain (Allam and Moghaddamjoo, 1994), we feel it is more natural for our problem to phase compensate plane wave events in the (f, p, q) domain obtained by 3-D plane wave decomposition using discrete Radon transforms.

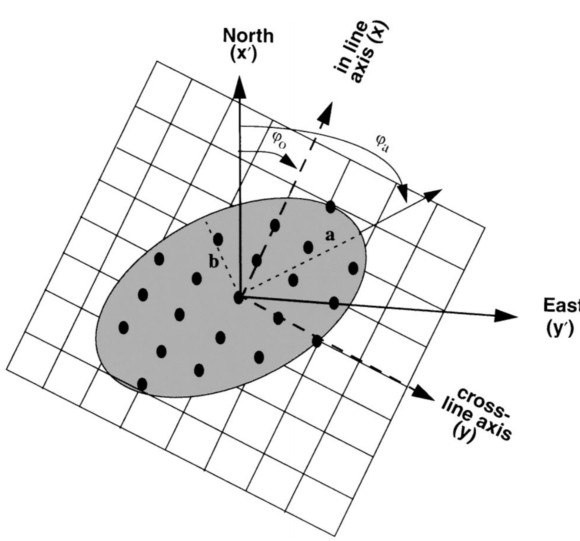

FIG. A-1. An elliptical analysis window centered about an analysis point defined by length of major axis a, length of minor axis b, and azimuth of major axis ϕ_a. The larger unshaded window is used in the phase compensation discussed in Appendix A.

We therefore take the least-squares discrete Radon transform of the windowed input data $\mathbf{d}_\ell$:

$$\mathbf{m}_\ell = \left(\mathbf{L}_\ell^{\mathbf{H}}\mathbf{L}_\ell + \varepsilon\mathbf{I}\right)^{-1}\mathbf{L}_\ell^{\mathbf{H}}\mathbf{d}_\ell, \tag{A-3}$$

where $d_\ell(m_x, m_y)$ is the ℓth Fourier transformed data component at frequency f_ℓ at position $(x = m_x\Delta x, y = m_y\Delta y)$; $m_\ell(n_p, n_q)$ are the (f, p, q) plane wave decomposition coefficients corresponding to ray parameters $(p = n_p\Delta p, q = n_q\Delta q)$, where $-N_p \le n_p \le +N_p$ and $-N_q \le n_q \le N_q$; $L_\ell(n_p, n_q, m_x, m_y) = \exp[-i2\pi f_\ell(n_p\Delta pm_x\Delta x + n_q\Delta qm_x\Delta y)]$ are the elements of the discrete Radon transform matrix; $\mathbf{L}_\ell^H$ denotes the complex conjugate transpose of $\mathbf{L}_\ell$; $\mathbf{I}$ is the $(2N_p + 1)(2N_q + 1)$ by $(2N_p + 1)(2N_q + 1)$ identity matrix; and ε is a small "prewhitening factor" used to stabilize the matrix inversion.

By choosing our 3-D analysis window to be a rectangular grid aligned with the in-line and cross-line seismic axes (Figure A-1), we achieve 3-D phase compensation results by cascading two efficient 2-D by 2-D Radon transforms. Such phase compensation in the plane wave domain is directly analogous to spatial data interpolation in the plane wave domain. Specifically, we take the plane wave coefficients generated from the data at f_ℓ and inverse discrete Radon transform back to the

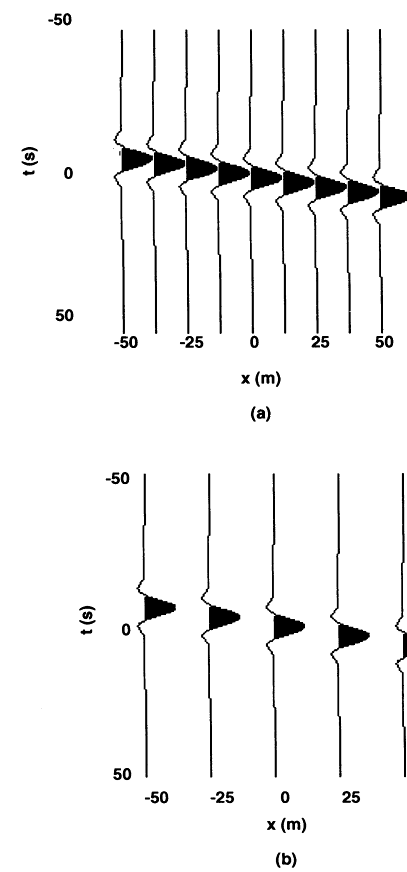

FIG. A-2. A planar reflector having an in-line dip of $p = 0.25$ ms/m, and a cross-line dip of $q = 0$ ms/m. Trace spacing is (a) 12.5 m and (b) 25 m.

(x, y) domain using the reference frequency f_R:

$$\bar{\mathbf{d}}_\ell = \mathbf{L}_R \mathbf{m}_\ell, \tag{A-4}$$

where $\bar{d}_\ell(m_x, m_y)$ is the data at frequency f_ℓ, phase compensated to frequency f_R, and

$$L_R(n_p, n_q, m_x, m_y) = \exp[-i2\pi f_R(n_p \Delta p m_x \Delta x + n_q \Delta q m_y \Delta y)]. \tag{A-5}$$

We therefore define our phase compensation matrix $\mathbf{D}_{\mathbf{R}\ell}$ to be

$$\mathbf{D}_{\mathbf{R}\ell} \equiv \mathbf{L}_R \left(\mathbf{L}_\ell^H \mathbf{L}_\ell + \varepsilon \mathbf{I}\right)^{-1} \mathbf{L}_\ell. \tag{A-6}$$

By applying $\mathbf{D}_{\mathbf{R}\ell}$ to each frequency component f_ℓ of a nonzero phase planar reflector centered at the origin, we minimize the phase difference, $\psi(f_R, x, y) - \psi(f_\ell, x, y)$, at all nonzero values of m_x and m_y:

$$\bar{\mathbf{d}}_\ell = \mathbf{D}_{\mathbf{R}\ell} \mathbf{d}_\ell. \tag{A-7}$$

We illustrate the effectiveness of the phase compensation operator $\mathbf{D}_{\mathbf{R}\ell}$ applied to the data in Figure A-2a in Figure A-4, where we have chosen a reference frequency $f_R = 50$ Hz. It appears that we are not able to correctly compensate the low-frequency component of the data at $f_\ell = 10$ Hz until our compensation window used in the discrete Radon transform exceeds a half analysis window size of 50 m (Figure A-4a). In contrast, if we choose a reference frequency of $f_R = 25$ Hz, we are able to accurately compensate the phase with a half analysis window size of 25 m (Figure A-5). If we draw an analogy between trace interpolation and phase compensation using discrete Radon transforms and look at the argument of equation (1) for a fixed value of apparent dips (p, q), we see that phase compensation of a frequency component that lies above the reference frequency f_R for a fixed (x, y) grid could alternatively be viewed as being interpolated to a finer (x, y) grid for the original frequency f_ℓ. Likewise, phase compensation of a frequency component that lies below the reference frequency f_R for a fixed (x, y) grid could alternatively be viewed as being extrapolated to a coarser (x, y) grid for the original frequency f_ℓ. Clearly, we know it is an unstable process to extrapolate data beyond the extent of the discrete Radon transform phase compensation window (Figure A-1), thereby explaining the poor results seen at 10 and 20 Hz in Figure A-4a. In contrast, the more stable

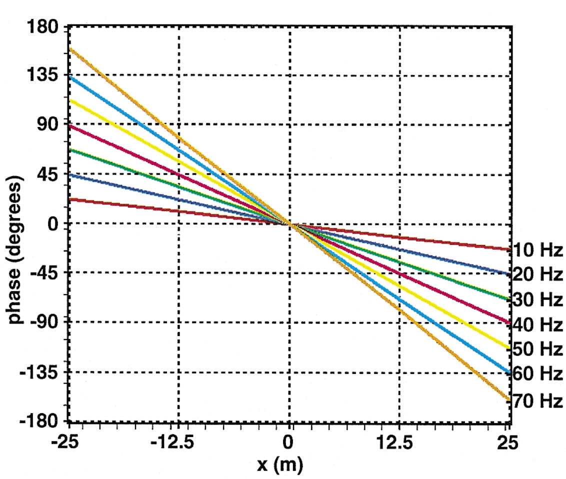

FIG. A-3. Phase as a function of frequency and distance from the center of the analysis window for the data shown in Figure A-2.

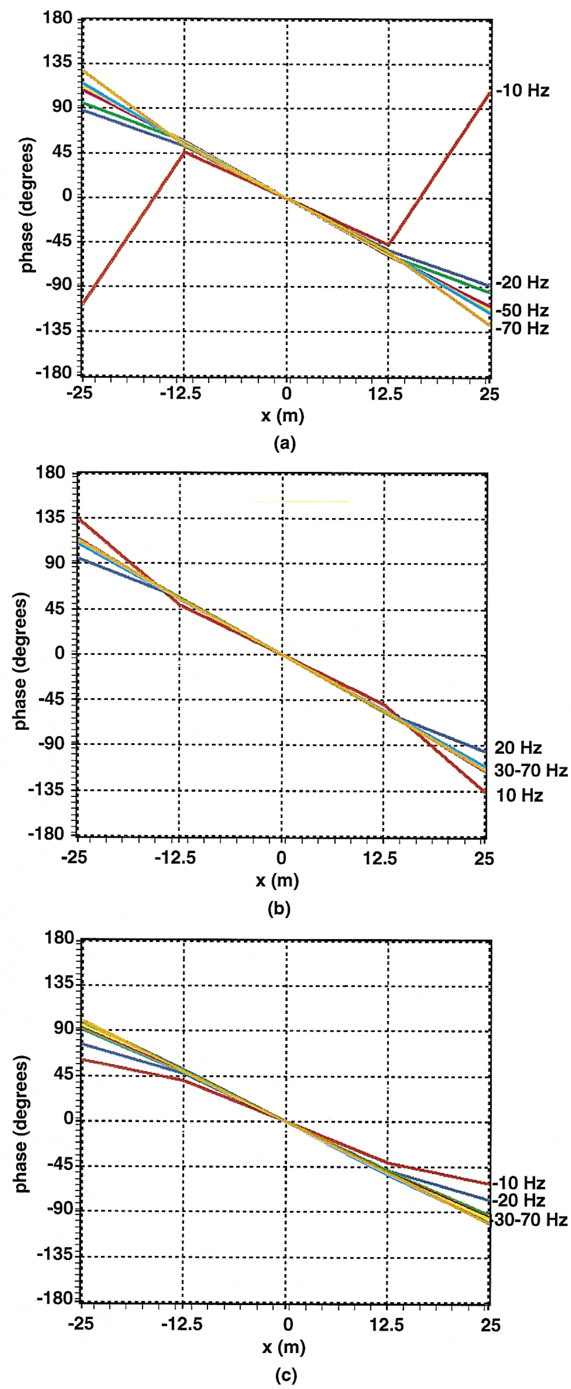

FIG. A-4. Phase compensation of the data shown in Figure A-2a with $\Delta x = 12.5$ m, using equation (A-7) and a reference frequency $f_R = 50$ Hz. Compensation windows used are (a) ± 25 m, (b) ± 37.5 m, and (c) ± 50 m.

process of interpolating the data grid towards the center of the analysis window makes the surrounding traces look more and more like the center trace, such that the compensated data will look more coherent as we lower the reference frequency. It appears that a reasonable compromise is to choose a reference

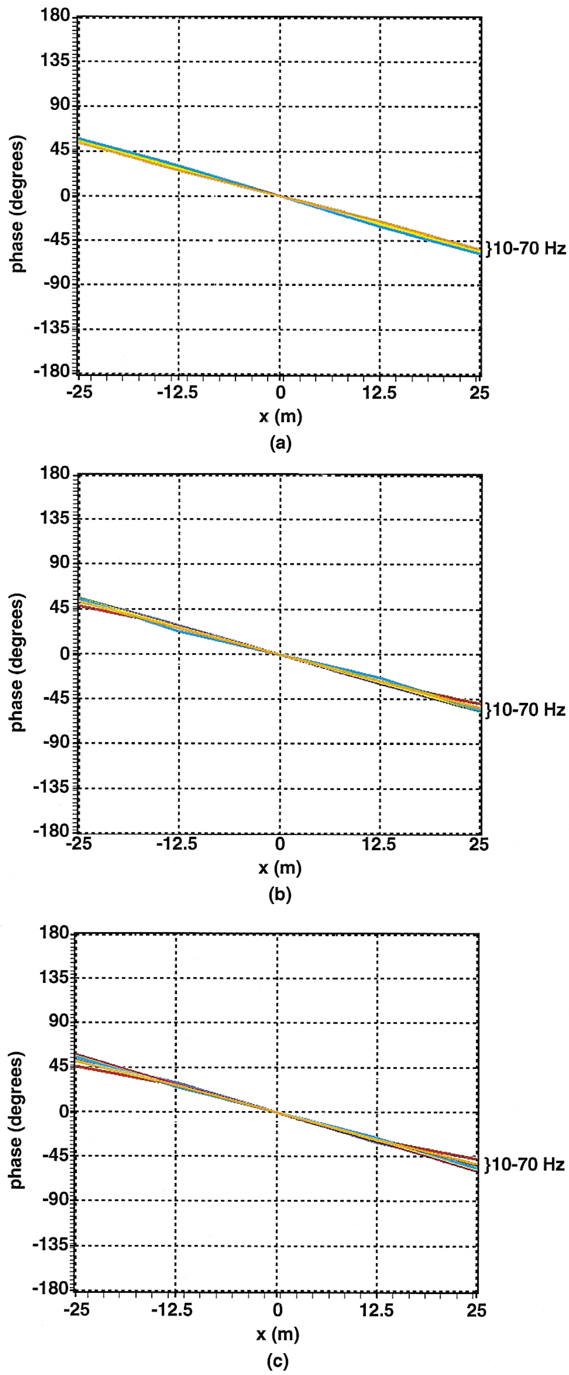

FIG. A-5. Phase compensation of the data shown in Figure A-2a with $\Delta x = 12.5$ m, using equation (A-7) and a reference frequency $f_R = 25$ Hz. Compensation windows used are (a) ± 25 m, (b) ± 37.5 m, and (c) ± 50 m.

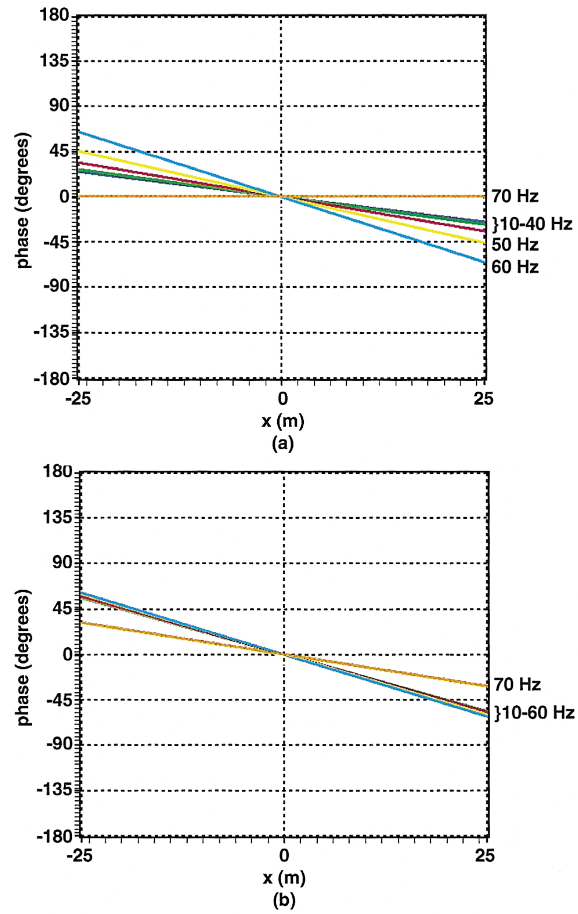

FIG. A-6. Phase compensation of the data shown in Figure A-2b with $\Delta x = 25$ m, using equation (A-7) and a reference frequency $f_R = 25$ Hz. Compensation windows used are (a) ± 25 m and (b) ± 50 m.

frequency that is near the center of the seismic spectrum, such as shown in Figure A-5, for a value of $f_R = 25$ Hz, where a phase compensation half window size equal to the analysis window of 25 m produces accurate results.

While the apparent dip of $p = 0.25$ ms/m is oversampled in Figure A-2a with a trace spacing of 12.5 m, it is only critically sampled at $f_\ell = 70$ Hz in Figure A-2b with a trace spacing of 25 m, a distance commonly used in 3-D seismic acquisition and processing. In Figure A-6, we note that the phase compensation algorithm breaks down if we use a phase compensation window equal to the coherence analysis half window of 25 m, even for frequencies higher than the reference frequency $f_R = 25$ Hz. We do achieve accurate phase compensation up to 60 Hz if we increase our analysis window by one additional trace in each direction, such that our phase compensation half window becomes 50 m. Although it is unclear exactly why the phase compensation breaks down for small windows, it is clear that increasing the phase compensation window to be larger than the coherence analysis window will mix in some amount of information from the larger window, thereby decreasing the lateral resolution of the coherence algorithm described in Appendix B.

APPENDIX B

FREQUENCY DOMAIN ESTIMATION OF COHERENCE

We can now use each of these phase compensated sample vectors at frequencies f_ℓ to create a broadband covariance matrix from which we will calculate coherence:

$$\mathbf{C}(p,q) = \sum_{\ell} \bar{\mathbf{d}}_{\ell}(m_x, m_y)\,\bar{\mathbf{d}}_{\ell}^{H}(m_x, m_y), \tag{B-1}$$

where the superscript H denotes the Hermitian or complex conjugate transpose of the phase compensated data vector $\bar{\mathbf{d}}_{\ell}$ calculated using equation (A-7).

The phase compensation described in Appendix A will ensure that plane wave events passing through the origin will add constructively for each frequency f_ℓ. Since the data are either time or depth migrated, we may assume that in the absence of coherent noise there is a single locally planar event having unknown apparent dips p and q. We can therefore construct test functions $\mathbf{r}$ having elements $r(m_x, m_y, p, q)$ associated with positions (m_x, m_y):

$$r(m_x, m_y, p, q) = \exp[i2\pi f_R(pm_x\Delta x + qm_y\Delta y)]. \tag{B-2}$$

In this case the noise-free covariance matrix $\mathbf{C}(p,q)$ has only one nonzero eigenvalue λ_1. Its associated eigenvector $\mathbf{v}_1$ has a vector exponential delay factor or phase $\psi(f_R, x, y)$, and elements identical to those of $r(m_x, m_y, p, q)$.

The Complex Semblance Algorithm

Once we have compensated for phase as a function of frequency, there are a number of means of estimating coherence in the frequency domain. The simplest means is to construct multiple test functions $\mathbf{r}_n$ for discrete values of (p_n, q_n) and compute an estimate of coherence, $c(p_n, q_n)$ using the inner product

$$c(p_n, q_n) = \frac{\mathbf{r_n^H}\mathbf{C}(p_n, q_n)\mathbf{r_n}}{J\,Tr(\mathbf{C})}, \tag{B-3}$$

where J is the length of the vector $\mathbf{r}_n$ and is equal to the number of seismic traces in the analysis window, and $Tr(\mathbf{C})$ denotes the numerical trace of the matrix $\mathbf{C}$, that is, the sum of its diagonal elements:

$$Tr(\mathbf{C}) = \sum_{j=1}^{J} C_{jj}.$$

Our estimate of reflector coherence corresponds to that apparent dip pair $(\hat{p}, \hat{q})$ for which the unnormalized coherence $\hat{c}$ is maximum. This is equivalent to the beam former or what we call the complex semblance algorithm, which is closely related to the time domain semblance algorithm presented by Marfurt et al. (1998).

The MUSIC Algorithm

A second, more precise method of estimating coherence uses the eigenvector outer product $\mathbf{v}_1\mathbf{v}_1^{\mathbf{H}}$ instead of $\mathbf{C}(p,q)$, where $\mathbf{v_1}$ is the eigenvector of $\mathbf{C}$ associated with the largest normalized eigenvalue λ_1. When there is no noise and only one plane

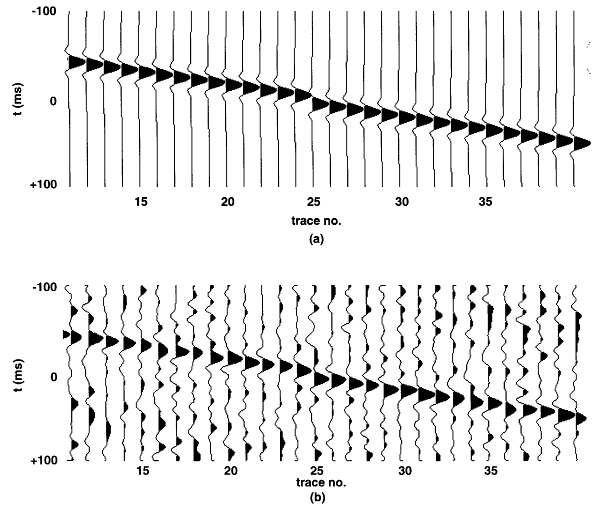

FIG. B-1. A planar reflector having an in-line dip of $p = 0.25$ ms/m and cross-line dip of 0.0 ms/m. Trace spacing $\Delta x = 12.5$ m. Offset of fault between trace 24 and 25 is $\Delta t = 10$ ms: (a) noise free, and (b) with a signal-to-noise ratio of 1:1.

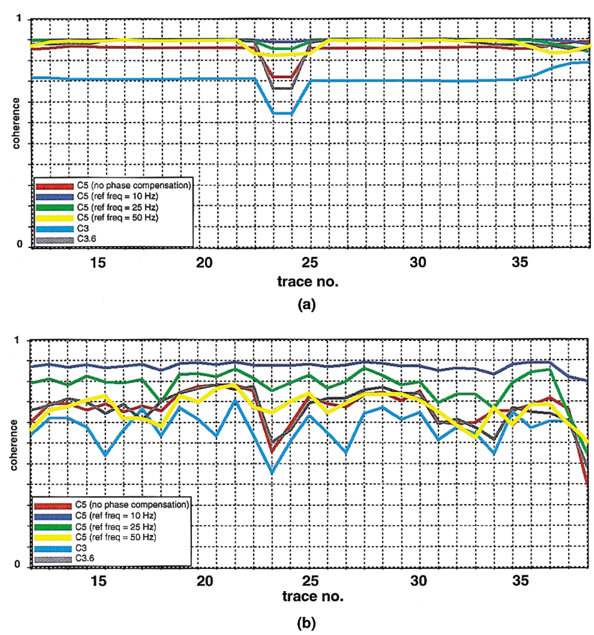

FIG. B-2. Coherence calculated using a ± 50 ms temporal and 3-trace spatial analysis window, corresponding to (a) the synthetic window noise shown in Figure B-1a, and (b) the synthetic with noise, shown in Figure B-1b.

wavefront,

$$\mathbf{v}_1\mathbf{v}_1^{\mathbf{H}} = \frac{\mathbf{C}}{Tr(\mathbf{C})}, \quad \text{(B-4)}$$

where, in this case (Parlett, 1980),

$$Tr(\mathbf{C}) = \sum_{j=1}^{J} \lambda_j = \lambda_1,$$

because all eigenvalues other than λ_1 are identically zero. The MUSIC algorithm (Wax et al., 1984) looks for a null or minimum in

$$c(p_n, q_n) = \mathbf{r}_\mathbf{n}^{\mathbf{H}}\left(\mathbf{I} - \mathbf{v}_1\mathbf{v}_1^{\mathbf{H}}\right)\mathbf{r}_\mathbf{n}, \quad \text{(B-5)}$$

usually by finding a peak in the inverse of this expression. For our work, we prefer the estimate

$$\hat{c} = \frac{\mathbf{r}^H(\hat{p}, \hat{q})\mathbf{v}_1\mathbf{v}_1^H\mathbf{r}(\hat{p}, \hat{q})}{J} \quad \text{(B-6)}$$

because it contains the same information and varies between 0 and 1 as the complex semblance does.

The MVDR Algorithm

The minimum variance, distortionless response (MVDR) algorithm, developed by Owsley (1985), finds a peak in the inverse of

$$c = \mathbf{r_n}^{\mathbf{H}}\mathbf{C}^{-1}\mathbf{r_n}. \quad \text{(B-7)}$$

At high signal-to-noise ratios, this algorithm is equivalent to MUSIC. Both MUSIC and MVDR have greater angular resolution and insensitivity to aliasing than the complex sembelnce algorithm. MVDR is more sensitive to noise than MUSIC, but less likely to give aliased solutions.

If there is only one reflector, the maximum coherence in the data can be given by

$$\hat{c} = \frac{\lambda_1}{\sum_{j=1}^{J}\lambda_j}.$$

Parlett (1980) and Golub and van Loan (1983) show this can be more efficiently calculated by noting that the sum of the eigenvalues is equal to numerical trace of the covariance matrix, while the largest eigenvalue can be efficiently calculated using the product method:

$$c = \frac{\lambda_1}{Tr(\mathbf{C})}. \quad \text{(B-8)}$$

We will denote this MVDR estimate of coherence as our C5 coherence algorithm and compare it to our time domain eigenstructure (C3.6) algorithm using the simple test synthetics of a dipping ($p = 0.25$ ms/m, $q = 0.0$ ms/m), faulted reflector (Figure B-1) used in Marfurt et al. (1999). We evaluate the effect of phase compensation on the noise-free synthetic displayed in Figure B-1b in Figure B-2a. We note that, as intended, the phase compensation brings the value of coherence up to $c = 1.0$ for the nonfaulted part of the reflector. For the C3.6 algorithm, the discontinuity associated with the fault between traces 24 and 25 gives rise to a drop in coherence localized to the bounding traces, thereby providing maximum resolution for a three-trace algorithm. Though the contrast in coherence is less, the MVDR algorithm without phase compensation is likewise optimally localized. The MVDR algorithm with phase compensation (i.e., our C5 algorithm) has values of coherence along the reflector and at the fault that mimic that of the C3.6 algorithm. Unfortunately, the effect of the phase compensation is to smooth the variation in coherence near the fault over the five-trace phase compensation window, thereby providing us with reduced lateral resolution. Decreasing the value of the reference frequency f_R from 50 Hz through 25 Hz to 10 Hz, we find that whereas the lateral resolution of the fault discontinuity increases with decreasing reference frequency, the overall coherence measured at the fault also increases such that the fault is difficult to recognize. As described in Appendix A, this increase in coherence for a low reference frequency can be explained by viewing the phase compensation operation as a trace interpolation operation, with the higher frequencies being interpolated closer and closer to, and therefore approaching the value of, the center of the analysis window.

In Figure B-2b, we make the same analysis for data having a signal-to-noise ratio of 1:1 within the bandwidth of the signal shown in Figure B-1b. Here, we note that our new frequency domain MVDR algorithm is less robust than the C3.6 time domain algorithm. To summarize Appendices A and B, it appears that while we are able to accurately compensate for the phase changes as a function of frequency and offset associated with dipping reflectors, in so doing we smooth out the very discontinuities we would like to map!